JOURNAL OF THE ROYAL SOCIETY Interface

J. R. Soc. Interface (2012) **9**, 1325–1338
doi:10.1098/rsif.2011.0605
Published online 23 November 2011

A validated predictive model of coronary fractional flow reserve

Yunlong Huo[1], Mark Svendsen[2], Jenny Susana Choy[1], Z.-D. Zhang[1] and Ghassan S. Kassab[1,*]

[1]*Department of Biomedical Engineering, Surgery, and Cellular and Integrative Physiology, Indiana University Purdue University Indianapolis (IUPUI), Indianapolis, IN 46202, USA*
[2]*Weldon School of Biomedical Engineering, Purdue University, West Lafayette, IN 47907, USA*

Myocardial fractional flow reserve (FFR), an important index of coronary stenosis, is measured by a pressure sensor guidewire. The determination of FFR, only based on the dimensions (lumen diameters and length) of stenosis and hyperaemic coronary flow with no other ad hoc parameters, is currently not possible. We propose an analytical model derived from conservation of energy, which considers various energy losses along the length of a stenosis, i.e. convective and diffusive energy losses as well as energy loss due to sudden constriction and expansion in lumen area. *In vitro* (constrictions were created in isolated arteries using symmetric and asymmetric tubes as well as an inflatable occluder cuff) and *in vivo* (constrictions were induced in coronary arteries of eight swine by an occluder cuff) experiments were used to validate the proposed analytical model. The proposed model agreed well with the experimental measurements. A least-squares fit showed a linear relation as $(\Delta p \text{ or FFR})_{\text{experiment}} = a(\Delta p \text{ or FFR})_{\text{theory}} + b$, where a and b were 1.08 and -1.15 mmHg ($r^2 = 0.99$) for *in vitro* Δp, 0.96 and 1.79 mmHg ($r^2 = 0.75$) for *in vivo* Δp, and 0.85 and 0.1 ($r^2 = 0.7$) for FFR. Flow pulsatility and stenosis shape (e.g. eccentricity, exit angle divergence, etc.) had a negligible effect on myocardial FFR, while the entrance effect in a coronary stenosis was found to contribute significantly to the pressure drop. We present a physics-based experimentally validated analytical model of coronary stenosis, which allows prediction of FFR based on stenosis dimensions and hyperaemic coronary flow with no empirical parameters.

Keywords: fractional flow reserve; lesion; coronary artery disease; Bernoulli's equation; model

1. INTRODUCTION

Myocardial fractional flow reserve (FFR), the ratio of distal to proximal pressure of a lesion under hyperaemic conditions [1], is an important index of coronary stenosis because it has lower variability and higher reproducibility than coronary flow reserve (CFR) and hyperaemic stenosis resistance (HSR) [2,3]. A recent landmark study showed a clear benefit of FFR in guiding percutaneous coronary intervention for better clinical outcome [4]. The current method for the measurement of FFR requires the use of a pressure wire inserted through the stenosis [2,3]. Although recent advancements in sensor guidewire technology allow simultaneous measurement of distal pressure and flow velocity, there are still high variability and instability of flow velocity, and occasional signal shift for pressure and guidewire obstruction of flow [2,3]. The placement of a pressure wire near a stenosis can also lead to overestimation of FFR. To avoid these procedural shortcomings and the expense of pressure wire, a non-invasive predictive validated model of FFR would be very valuable.

Although angiographically based methods for the measurement of coronary flow [5,6] and lesion dimension [7,8] have been well established, there is still a lack of fundamental theory that can determine the pressure drop (Δp) and hence FFR, based on the dimension of lesion (i.e. the cross-sectional area-CSA along the lesion and the length of lesion) and hyperaemic coronary flow with no empirical parameters. The objective of this study is to introduce such a predictive analytical model and to validate it using *in vitro* and *in vivo* experiments and finite-element (FE) method.

In vessel segments without a stenosis, the pressure–flow curve is nearly linear in the physiological pressure range during maximal vasodilation [9]. The linear pressure–flow relation is altered when stenosis is present [10]. Young and co-workers [11–14] showed a quadratic relation between pressure gradient and flow rate as $\Delta p = AQ + BQ^2$, where A and B were empirical parameters determined through a curve fit of experimental data. Although the quadratic relation was experimentally validated for coronary stenosis [10],

*Author for correspondence (gkassab@iupui.edu).

Received 7 September 2011
Accepted 3 November 2011

the empirical parameters (A and B) are not known *a priori* [15]. Hence, there is a need for a model of Δp or FFR that does not contain any empirical parameters, but only depends on measurable quantities of coronary artery lesion.

Here, we present an analytical model derived from the general Bernoulli equation (conservation of energy), which considers various energy losses along the length of a lesion. The input model variables are lesion lumen CSA (the proximal, distal and minimal CSA along the lesion), and the length of lesion and hyperaemic volumetric flow rate through the lesion. There are no empirical parameters in the analytical model unlike previous models [11–14]. The *in vitro* and *in vivo* experiments (swine) as well as a Galerkin FE model were used to validate the proposed analytical model. The significance, limitations and implications of the validated model are contemplated.

2. METHODS

2.1. Analytical model

Myocardial FFR is a functional parameter of stenosis severity. FFR during hyperaemic flow is expressed as

$$\mathrm{FFR} = \frac{P_{\mathrm{distal}} - P_{\mathrm{v}}}{P_{\mathrm{a}} - P_{\mathrm{v}}}, \tag{2.1}$$

where P_{a} is the mean aortic pressure ($P_{\mathrm{a}} \approx P_{\mathrm{proximal}}$ assuming a proximal lesion or no significant diffuse coronary artery disease in a distal lesion); P_{v} is the central venous pressure; P_{proximal} and P_{distal} are the hyperaemic coronary pressure proximal and distal to stenosis, respectively [1]. If the central venous pressure is assumed to be negligible, equation (2.1) is generally approximated as

$$\mathrm{FFR} = \frac{P_{\mathrm{distal}}}{P_{\mathrm{a}}} = \frac{P_{\mathrm{a}} - \Delta p}{P_{\mathrm{a}}}, \tag{2.2}$$

where Δp is the pressure gradient along the axis of vessel segment from proximal to distal position of stenosis.

Here, we propose a model to determine Δp specifically for the coronary arteries (see details in appendix A). Briefly, since gravity is negligible in the coronary circulation [16], the general Bernoulli equation can be written as

$$\Delta P = \Delta P_{\mathrm{convective}} + \Delta P_{\mathrm{constriction}} + \Delta P_{\mathrm{diffusive}} + \Delta P_{\mathrm{expansion}}, \tag{2.3}$$

$\Delta P_{\mathrm{convective}}$, $\Delta P_{\mathrm{constriction}}$, $\Delta P_{\mathrm{diffusive}}$ and $\Delta P_{\mathrm{expansion}}$ are energy losses due to flow convection, sudden constriction in CSA from proximal normal vessel to stenosis, flow diffusion and sudden expansion in CSA from stenosis to distal normal vessel, respectively.

$$\Delta P_{\mathrm{convective}} = \frac{\rho Q^2}{2}\left(\frac{1}{\mathrm{CSA}_{\mathrm{outlet}}^2} - \frac{1}{\mathrm{CSA}_{\mathrm{inlet}}^2}\right),$$

where $\mathrm{CSA}_{\mathrm{inlet}}$ and $\mathrm{CSA}_{\mathrm{outlet}}$ are the inlet and outlet cross-sectional areas, respectively; Q is the hyperaemic flow rate in a vessel segment; ρ is the density of blood. If the flow transition, from proximal normal vessel to stenosis, is well-bound and follows the streamlines, the energy loss due to a sudden constriction is relatively small (loss coefficient $\ll 0.1$ generally) and negligible such that $\Delta P_{\mathrm{constriction}} = 0$.

Although $\Delta P_{\mathrm{diffusive}}$ is generally caused by the viscosity in the fully developed region (i.e. viscous energy loss in this case), the pressure drop serves both to accelerate the flow and to overcome viscous drag in the entrance region of a stenosis, which contributes to the diffusive energy loss. For the entrance region of stenosis, we define a dimensionless radius of inviscid core (α), in which the flow velocity is uniform such as $\alpha = r$ at the inlet, $0 < \alpha < r$ from the inlet to the fully developed region and $\alpha = 0$ at the fully developed region, as shown in figure 6*a–c*, respectively. The dimensionless radius of inviscid core (α) is calculated from

$$\frac{\pi\mu L_{\mathrm{stenosis}}}{4\rho Q} = \frac{1}{4}\int_{\alpha}^{1} \frac{(1-\alpha)(6+\alpha)(1+4\alpha+9\alpha^2+4\alpha^3)}{5\alpha(3+2\alpha)(3+2\alpha+\alpha^2)^2}\,\mathrm{d}\alpha,$$

where L_{stenosis} is the length of stenosis [17]. L_{vessel} is the length of vessel, which is composed of both normal vessel and stenosis. If $\alpha \geq 0.05$ (most common for coronary artery dimensions and lesion lengths), $\Delta P_{\mathrm{diffusive}}$ and $\Delta P_{\mathrm{expansion}}$ are expressed as

$$\Delta P_{\mathrm{diffusive}}^{\alpha \geq 0.05} = \frac{\rho Q^2}{2\mathrm{CSA}_{\mathrm{stenosis}}^2}\frac{96}{5}\int_{\alpha}^{1} \frac{(1+4\alpha+9\alpha^2+4\alpha^3)}{\alpha(3+2\alpha)(3+2\alpha+\alpha^2)^2}\,\mathrm{d}\alpha + \int_{0}^{L_{\mathrm{vessel}}-L_{\mathrm{stenosis}}} \frac{8\pi\mu}{\mathrm{CSA}^2}\,Q\,\mathrm{d}x$$

and

$$\Delta P_{\mathrm{expansion}}^{\alpha \geq 0.05} = \frac{\rho Q^2}{2}\left\{\left(\frac{1}{\mathrm{CSA}_{\mathrm{stenosis}}} - \frac{1}{\mathrm{CSA}_{\mathrm{distal}}}\right)^2 + \left[2\left(\frac{1}{\mathrm{CSA}_{\mathrm{stenosis}}} - \frac{1}{\mathrm{CSA}_{\mathrm{distal}}}\right)\times\left(\frac{1}{\mathrm{CSA}_{\mathrm{stenosis}}} - \frac{1}{3}\frac{1}{\mathrm{CSA}_{\mathrm{distal}}}\right) - \left(\frac{1}{\mathrm{CSA}_{\mathrm{stenosis}}} - \frac{1}{\mathrm{CSA}_{\mathrm{distal}}}\right)^2\right](1-\alpha)^2\right\}.$$

If $\alpha < 0.05$, the entire stenosis is divided into entrance and fully developed regions, and the entrance length L_{entrance} is obtained from

$$\frac{\pi\mu L_{\mathrm{entrance}}}{4\rho Q} = \frac{1}{4}\int_{0.05}^{1} \frac{(1-\alpha)(6+\alpha)(1+4\alpha+9\alpha^2+4\alpha^3)}{5\alpha(3+2\alpha)(3+2\alpha+\alpha^2)^2}\,\mathrm{d}\alpha,$$

such that

$$\Delta P_{\mathrm{diffusive}}^{\alpha < 0.05} = \frac{\rho Q^2}{2\mathrm{CSA}_{\mathrm{stenosis}}^2}\frac{96}{5}\int_{0.05}^{1} \frac{(1+4\alpha+9\alpha^2+4\alpha^3)}{\alpha(3+2\alpha)(3+2\alpha+\alpha^2)^2}\,\mathrm{d}\alpha + \int_{0}^{L_{\mathrm{vessel}}-L_{\mathrm{entrance}}} \frac{8\pi\mu}{\mathrm{CSA}^2}\,Q\,\mathrm{d}x$$

and $$\Delta P_{\mathrm{expansion}}^{\alpha < 0.05} = \rho Q^2\left(\frac{1}{\mathrm{CSA}_{\mathrm{stenosis}}} - \frac{1}{\mathrm{CSA}_{\mathrm{distal}}}\right)\times\left(\frac{1}{\mathrm{CSA}_{\mathrm{stenosis}}} - \frac{1}{3}\frac{1}{\mathrm{CSA}_{\mathrm{distal}}}\right).$$

Table 1. Geometrical parameters and flow rates in blood vessel and stenosis of *in vitro* experiments.

stenosis set-ups	stenotic diameters (mm)	stenotic lengths (mm)	normal vessel diameters (mm)	flow rates ($\mathrm{ml\,s^{-1}}$)
symmetric long tubing	2.1	110	3.7	1.3, 1.7 or 2.1
symmetric tubings	0.85, 1.2 or 1.7	10–30	3.5–5	1.1, 1.7, 2.3 or 2.7
asymmetric tubings	0.85 or 1.3	8–22		
occluder cuff	1.25, 1.65 or 2	5		

Here, the entrance effect plus the viscosity (Poiseuille formula in the fully developed region) leads to the diffusive energy loss. We also account for the energy loss due to a sudden expansion in CSA, based on the outlet flow pattern that represents the growth of the boundary layer from the inlet of stenosis to the outlet. Equation (2.3) was combined with equation (2.2) to determine FFR from the stenosis geometry and hyperaemic flow.

We also compared the present model (equation (2.3)) with other models that do not consider the entrance effect [13,14,18]:

$$\Delta P_{\mathrm{theory}}^{\mathrm{no\,entrance}} = \frac{\rho Q^2}{2}\left(\frac{1}{\mathrm{CSA}_{\mathrm{outlet}}^2} - \frac{1}{\mathrm{CSA}_{\mathrm{inlet}}^2}\right) + \Delta P_{\mathrm{diffusive}}^{\mathrm{no\,entrance}} + \Delta P_{\mathrm{expansion}}^{\mathrm{no\,entrance}}. \quad (2.4)$$

If the entrance effect is omitted,

$$\Delta P_{\mathrm{diffusive}}^{\mathrm{no\,entrance}} = \int_0^{L_{\mathrm{vessel}}} \frac{8\pi\mu}{\mathrm{CSA}^2}\, Q\, \mathrm{d}x.$$

The energy loss due to a sudden expansion can be modelled as:

$$\Delta P_{\mathrm{expansion}}^{\mathrm{no\,entrance}} = \frac{\rho Q^2}{2}\left(\frac{1}{\mathrm{CSA}_{\mathrm{stenosis}}} - \frac{1}{\mathrm{CSA}_{\mathrm{distal}}}\right)^2$$

(uniform outlet velocity),

$$\Delta P_{\mathrm{expansion}}^{\mathrm{no\,entrance}} = 1.52 \times \frac{\rho Q^2}{2}\left(\frac{1}{\mathrm{CSA}_{\mathrm{stenosis}}} - \frac{1}{\mathrm{CSA}_{\mathrm{distal}}}\right)^2$$

(the product of a constant and uniform outlet velocity) [13] or

$$\Delta P_{\mathrm{expansion}}^{\mathrm{no\,entrance}} = \frac{\rho Q^2}{2}\left(\frac{1}{\mathrm{CSA}_{\mathrm{stenosis}}} - \frac{1}{\mathrm{CSA}_{\mathrm{distal}}}\right) \times \left(\frac{1}{\mathrm{CSA}_{\mathrm{stenosis}}} - \frac{1}{3}\frac{1}{\mathrm{CSA}_{\mathrm{distal}}}\right)$$

(parabolic outlet velocity).

2.2. Validation

A Galerkin FE model was compared with the analytical model of equation (2.3). The Navier–Stokes equations were solved for velocity and pressure subject to a non-slip wall boundary condition and a stress-free outlet boundary condition [19,20]. The axisymmetric control volume was a rectangle of vessel radius × vessel length (0.15 × 6 cm). After a mesh-independent test, the control volume was divided into 20 × 200 quadrilateral and hybrid FEs for healthy and stenotic vessels, respectively. The viscosity (μ) and density (ρ) of the solution were selected as 4.5 cp and $1.06\,\mathrm{g\,cm^{-3}}$, respectively, to mimic blood flow with a haematocrit of about 45 per cent in medium size arteries. Various dimensions of stenosis (area stenosis varying from 20 to 90% and length of stenosis from 0.5 to 2 cm) and flow velocities ($5–50\,\mathrm{cm\,s^{-1}}$) were used to calculate the pressure drop.

In vitro and *in vivo* experiments were used to validate the analytical model of pressure drop (equation (2.3)) and FFR (equation (2.2)). The dimensions of the stenosis and flow rates for *in vitro* and *in vivo* experiments are listed in tables 1 and 2, respectively. The prediction of other models ($\Delta P_{\mathrm{diffusive}}^{\mathrm{no\,entrance}}$ in equation (2.4)) was also compared with the measurements. Studies were performed on eight domestic swine weighing 60–70 kg.

Surgical anaesthesia was induced with TKX (Telazol 500 mg, ketamine 250 mg, xylazine 250 mg) and maintained with 2 per cent isoflurane [21]. The animal was intubated and ventilated with room air and oxygen by a respiratory pump. A side branch from the left jugular vein was dissected and cannulated with a 7 Fr sheath for administration of drugs (e.g. heparin, lidocaine, levophed and saline as needed). The right femoral artery was cannulated with a 7 Fr sheath and then a guide catheter was inserted to measure the aortic blood pressure using a transducer (Summit Disposable Pressure Transducer, Baxter Healthcare; error of ±2% at full scale).

For the *in vitro* experiments, carotid arteries were dissected and isolated, and small side branches were ligated by suture. Several tubings (concentric and eccentric) and an inflatable occluder cuff (OC4, *In Vivo* Metric) were used to create various stenoses (figure 1*a*,*b*). In one *in vitro* set-up, various sizes of concentric and eccentric tubings were inserted into carotid artery and ligated against the vessel wall to form symmetric and asymmetric stenoses, as shown in figure 1*a*. Table 1 shows the geometry and flow rate in carotid arteries and tubings. The stenosis eccentricity ranged from zero to 0.8 (defined as $D_{\mathrm{axis}}/R_{\mathrm{proximal}}$, where D_{axis} is the distance of centrelines between stenosis and proximal vessel segment and R_{proximal} is the radius of the proximal vessel segment to stenosis).

In another *in vitro* set-up, an arterial occluder was mounted around the carotid artery to create stenoses of different degrees (as shown in figure 1*b*). The occluder cuff has an inner diameter and length of 4 mm and 5 mm, respectively, which can induce zero

Table 2. Geometrical parameters and flow rates in blood vessel and stenosis of *in vivo* experiments. The stenotic length is 5 mm.

coronary stenoses	stenotic diameters (mm)	normal vessel diameters (mm)	flow rates ($ml\,s^{-1}$)	aortic pressure (mmHg)
LAD stenosis 1	2.1	3.8	3.27	69.1
LAD stenosis 2	2.3	3.8	3.52	71.6
LAD stenosis 3	1.4	4.1	2.43	67.3
LAD stenosis 4	1.6	4.3	2.88	76
LAD stenosis 5	1.4	3.3	2.31	62.7
LAD stenosis 6	1.3	3.3	1.73	63.6
LAD stenosis 7	1.4	4.5	1.57	66
LAD stenosis 8	1.7	4.0	3.05	70
LAD stenosis 9	1.2	3.5	1.59	66.6
RCA stenosis 1	1.2	3.7	1.6	72.6
RCA stenosis 2	1.2	3.7	1.1	66
RCA stenosis 3	1.1	3.9	0.97	62.4
RCA stenosis 4	1.4	4.6	1.41	58.3
RCA stenosis 5	1.3	4.6	1.39	62
RCA stenosis 6	1.3	4.5	1.57	60
RCA stenosis 7	1.4	4.5	1.9	59.5
RCA stenosis 8	1.4	4.7	2.17	62.1
RCA stenosis 9	1.4	4.7	2.36	76
RCA stenosis 10	1.3	4.7	1.79	64.5
RCA stenosis 11	1.2	3.5	1.39	60.5

(no stenosis) to unity (full stenosis) area stenoses. The volumetric flow rate (Q) was measured by a perivascular flow probe (Transonic Systems Inc.; a relative error of $\pm 2\%$ at full scale). The arteries were cannulated to T-junctions at both ends. The pressure transducers were connected to the T-junctions to measure the proximal and distal pressures (P_{proximal} and P_{distal}, respectively) of the stenosis in order to determine the pressure gradient ($\Delta p = P_{\text{proximal}} - P_{\text{distal}}$). Pulsatile pressure and flow were continuously recorded using a Biopac MP 150 data acquisition system (Biopac Systems, Inc., Goleta, CA). A cast was made at 100 mmHg after the stenotic vessel was fixed with 6.25 per cent glutaraldehyde solution in 0.1 sodium cacodylate buffer (osmolarity of fixative was 1100 mosM) [22]. Photographs of small rings sectioned from the vessel and stenosis casts were then taken (figure 1*b*). The CSA measurements were made using the NIS-Elements imaging software for the cast.

For the *in vivo* experiments, the analytical model was validated in coronary arteries. A sheath was introduced through the femoral artery to access the right coronary artery (RCA), left anterior descending artery (LAD artery) and left circumflex artery (LCx artery). After a midline sternotomy, the main trunk of these arteries was dissected free from the surrounding tissue in preparation for the placement of a flow probe and an inflatable occluder with no apparent major branches in between them. The coronary artery was gradually occluded by an inflatable occluder cuff to create different degrees of stenoses. The hyperaemic volumetric flow rate (intracoronary injection of adenosine: 120 μg for both left and right coronary arteries) was determined by a flow probe (Transonic Systems Inc.; a relative error of $\pm 2\%$ at full scale). The distal pressure to coronary stenosis (P_{distal}) was measured by a Volcano ComboWire (Volcano Corp., San Diego, CA, USA), which was inserted into the coronary artery through a sheath. The proximal, distal and minimal CSAs were obtained from coronary angiograms, using previous method [7,8].

2.3. Data analysis

The proximal, distal and minimal CSA and stenosis length as well as hyperaemic flow rate were used to calculate the pressure drop (equation (2.3)), which was compared with the measurement obtained from *in vitro* and *in vivo* experiments. The relation of the pressure drop between the analytical (or theoretical) model and experimental measurements was expressed as $\Delta P_{\text{experiment}} = a\Delta P_{\text{theory}} + b$. Myocardial FFR was calculated from the theoretical model (a combination of equations (2.2) and (2.3)) in comparison with the *in vivo* coronary measurements. The empirical constants, a and b, were determined by a linear least-squares fit with corresponding correlation coefficients (r^2). In a Bland–Altman diagram, the difference of pressure drop and myocardial FFR between the theoretical model and experimental measurements was plotted against their means. In the scatter diagram, the precision and bias of the analytical model were quantified. We also determined the root mean square error (r.m.s.e.) to further assess the accuracy of the theoretical model.

2.4. Sensitivity analysis

To determine the sensitivity of the model to various inputs (e.g. CSA and length of the lesion, hyperaemic flow), we varied these parameters over a range of values and determined the effect on pressure drop. The normalized pressure drop ($(\Delta P_{\text{perturbed}} - \Delta P_{\text{actual}})/(\Delta P_{\text{actual}})$) was determined as a function of parameter $X((X_{\text{perturbed}} - X_{\text{actual}})/(X_{\text{actual}}))$, which refers to distal

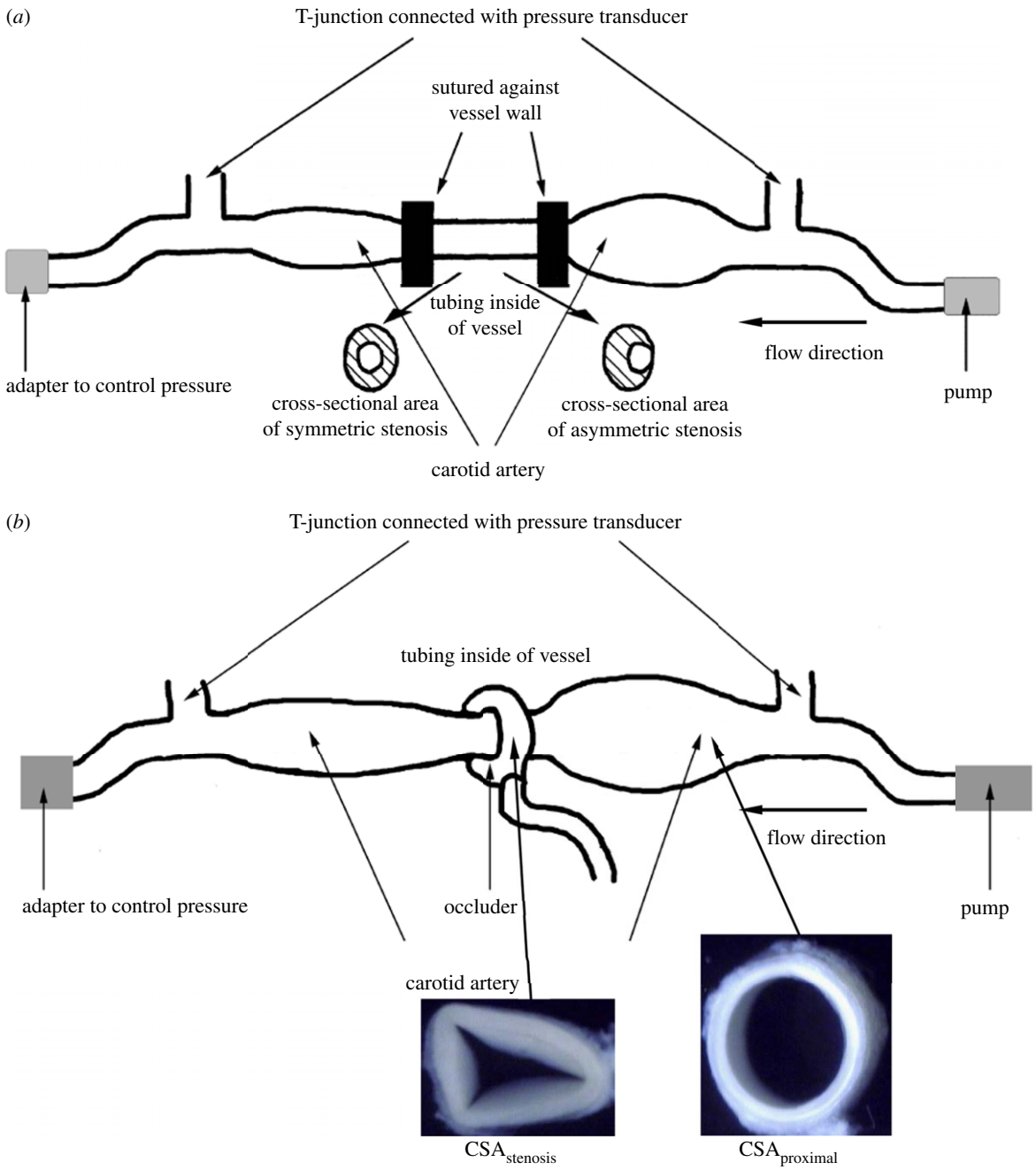

Figure 1. (*a*–*b*) Schematic of *in vitro* stenosis set-ups: (*a*) insertion of known sizes of concentric and eccentric tubings into carotid artery to mimic various stenoses; (*b*) an inflatable arterial occluder to create various stenoses.

CSA, stenosis CSA, stenosis length and flow rate in a vessel (actual or reference values of $(\pi 4.5^2/4)\ \mathrm{mm}^2$, $(\pi 1.7^2/4)\ \mathrm{mm}^2$, 10 mm and 111 ml min^{-1}). The proximal CSA was not considered, as it has a negligible effect on pressure drop. The actual pressure drop ($\Delta P_{\mathrm{actual}}$) equalled to 9.4 mmHg when the dynamic viscosity of blood is 4.5 cp. The perturbed pressure drop ($\Delta P_{\mathrm{perturbed}}$) was calculated by equation (2.3) when X_{actual} was changed to $X_{\mathrm{perturbed}}$.

3. RESULTS

A comparison of pressure drop between the theoretical model (equation (2.3)) and FE simulation shows a linear relation as $\Delta P_{\mathrm{FE\ \ model}} = 0.98\Delta P_{\mathrm{theory}} - 0.14$ ($r^2 = 1$). Figure 1 shows the *in vitro* stenosis set-up in the carotid artery using concentric and eccentric tubings as well as an inflatable occluder cuff, the dimensions of which are shown in table 1. The flow rates were varied in the range of 65–170 ml min^{-1}. Figure 2*a* shows a comparison of pressure gradient between the present theoretical model (i.e. equation (2.3)) and *in vitro* experiments, which has the linear relation $\Delta P_{\mathrm{experiment}} = 1.08\Delta P_{\mathrm{theory}} - 1.15$ ($r^2 = 0.99$) (table 3). Moreover, the difference of pressure gradients ($\Delta P_{\mathrm{theory}} - \Delta P_{\mathrm{experiment}}$) was plotted against the mean value ($(\Delta P_{\mathrm{theory}} + \Delta P_{\mathrm{experiment}})/2$), as shown in figure 2*b*. The mean systematic error (or bias) of the difference of pressure drops (−0.59 mmHg) was nearly zero, which suggests consistency of the theoretical model and experimental measurements. Therefore, the

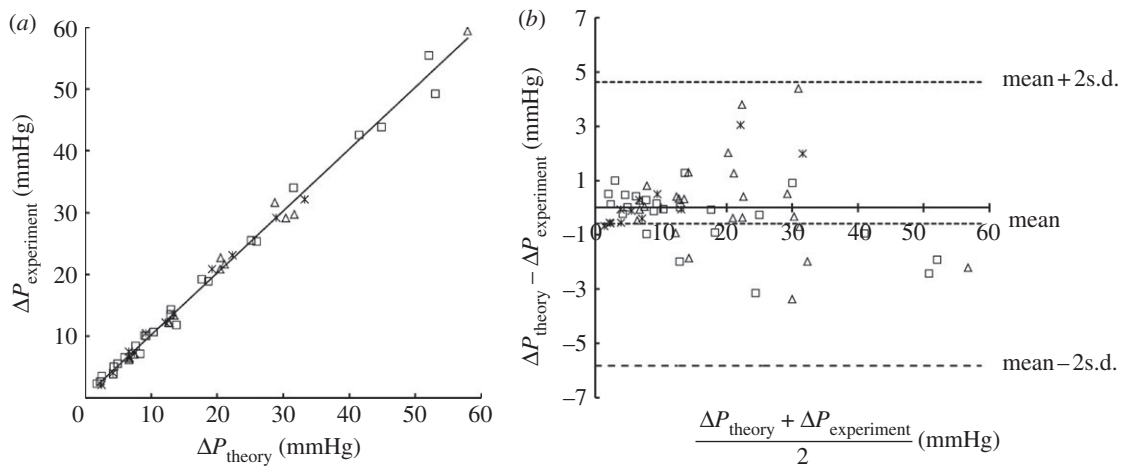

Figure 2. (*a*) A comparison of pressure gradient between theoretical model (i.e. equation (2.3)) and *in vitro* carotid experiments (ΔP_{theory} versus $\Delta P_{experiment}$) using symmetric (squares) and asymmetric (triangles) tubings as well as an inflatable occluder cuff (asterisks). A least-squares fit shows a relation: $\Delta P_{experiment} = 1.08 \times \Delta P_{theory} - 1.15$ ($r^2 = 0.99$). (*b*) Bland–Altman plots for the pairwise comparisons of pressure gradient between theoretical model and *in vitro* experiments, where the mean ± s.d. of pressure gradient difference ($\Delta P_{theory} - \Delta P_{experiment}$) are −0.59 and 2.61 mmHg, which is not significantly different from zero ($p \gg 0.05$). The r.m.s.e. of pressure gradient difference between theoretical model and *in vitro* experiments is 2.66 mmHg. The dynamic viscosity of saline solution is 1.0 cp.

Table 3. A comparison of the present model (equation (2.3)) with other models that do not consider the entrance effect (equation (2.4)), and *in vitro* experimental measurements $\Delta P_{theory} - \Delta P_{experiment}$. A least-squares fit was used to determine parameters for $\Delta P_{experiment} = a\Delta P_{theory} + b$ and $\Delta P_{experiment} = a\Delta P_{theory}^{no\ entrance} + b$.

model	a	b	r^2	mean systematic error (or bias)	r.m.s.e.
present model (equation (2.3))	$\Delta P_{experiment} = a\Delta P_{theory} + b$			$\Delta P_{theory} - \Delta P_{experiment}$ (mmHg)	
	1.08	−1.15	0.99	−0.59	2.66
other models (equation (2.4)) with different outlet flow patterns	$\Delta P_{experiment} = a\Delta P_{theory}^{no\ entrance} + b$			$\Delta P_{theory}^{no\ entrance} - \Delta P_{experiment}$ (mmHg)	
uniform outlet velocity	1.98	−0.72	0.99	−10.0	15.3
a constant (1.52) times uniform outlet velocity	1.45	−0.77	0.98	−6.04	9.79
parabolic outlet velocity	1.21	−1.28	0.95	−1.82	5.37

1 s.d. value (2.61 mmHg) was similar to the r.m.s.e. (2.66 mmHg) for the pressure difference. Figure 2 shows a good correlation between ΔP_{theory} and $\Delta P_{experiment}$. It should be noted that the pressure drop was accurately predicted by the model in comparison with experiments for various stenotic segments (concentric, eccentric, cuff and various lengths).

A comparison of pressure drop between other analytical models (i.e. equation (2.4)) and *in vitro* experiments is shown in table 3. The experimental results were more in agreement with the proposed model (equation (2.3)) when both entrance effects at the inlet of stenosis and flow velocity profiles at the outlet of stenosis were considered and hence all subsequent calculations accounted for those factors. A comparison of *in vitro* pulsatile and steady-state flows shows a relative error of pressure drop less than ±5% so that the time-averaged flow rate (over a cardiac cycle) is used in equation (2.3) for determination of pressure drop for the relatively small Womersley and Reynolds numbers in coronary arteries.

Figure 3*a* shows a comparison of pressure drop between the theoretical model (equation (2.3)) and *in vivo* coronary experiments (ΔP_{theory} versus $\Delta P_{experiment}$), whose geometrical and haemodynamic parameters are listed in table 2. A linear least-squares fit yielded a relation as $\Delta P_{experiment} = 0.96\Delta P_{theory} + 1.79$ ($r^2 = 0.75$). Figure 3*b* shows a Bland–Altman plot for the pairwise comparisons of pressure drop between the theoretical model and *in vivo* experiments, where the mean of pressure difference ($\Delta P_{theory} - \Delta P_{experiment}$) was −1.01, which was not significantly different from zero ($p \gg 0.05$). The r.m.s.e. of pressure difference between the theoretical model and *in vivo* experiments was 3.65 mmHg.

Figure 4*a* shows the relationship of FFR between the theoretical model (a combination of equations (2.2) and (2.3)) and *in vivo* coronary experiments (FFR_{theory} versus $FFR_{experiment}$), expressed as $FFR_{experiment} = 0.85FFR_{theory} + 0.1$ ($r^2 = 0.7$). Myocardial FFR was found to be less than 0.8 when the area stenosis was greater than 75 per cent (where $CSA_{proximal}$ is in the range of $(\pi/4)3.3^2 - (\pi/4)4.7^2$ mm^2). Similar to the

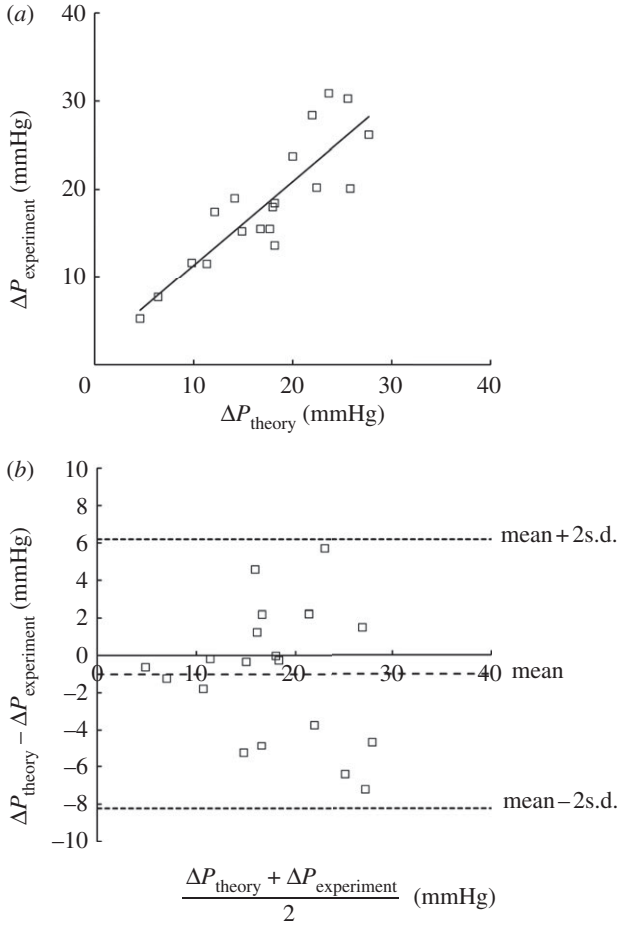

Figure 3. (*a*) A comparison of pressure gradient between theoretical model (i.e. equation (2.3)) and *in vivo* coronary experiments (ΔP_{theory} versus $\Delta P_{experiment}$). A linear least-squares fit shows a relation: $\Delta P_{experiment} = 0.96\Delta P_{theory} + 1.79$ ($r^2 = 0.75$). (*b*) Bland–Altman plots for the pairwise comparisons of pressure gradient between theoretical model and *in vivo* coronary experiments, where the mean ± s.d. of pressure gradient difference ($\Delta P_{theory} - \Delta P_{experiment}$) are −1.01 and 3.6 mmHg, which is not significantly different from zero ($p \gg 0.05$). The r.m.s.e. of pressure gradient difference between theoretical model and *in vivo* experiments is 3.65 mmHg. The dynamic viscosity of blood flow is 4.5 cp.

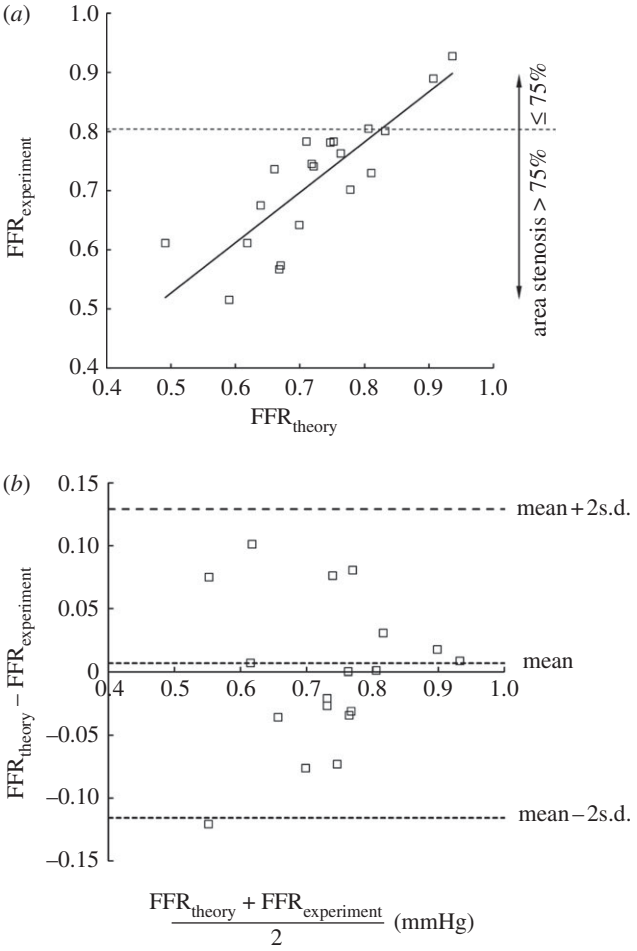

Figure 4. (*a*) A comparison of myocardial FFR between theoretical model (equations (2.2) and (2.3)) and *in vivo* coronary experiments (FFR_{theory} versus $FFR_{experiment}$). A least-squares fit shows a relation: $FFR_{experiment} = 0.85FFR_{theory} + 0.1$ ($r^2 = 0.7$). (*b*) Bland–Altman plots for the pairwise comparisons of myocardial FFR between theoretical model and *in vivo* coronary experiments, where the mean ± s.d. of myocardial FFR difference ($FFR_{theory} - FFR_{experiment}$) are 0.01 and 0.06, which is not significantly different from zero ($p \gg 0.05$). The r.m.s.e. of myocardial FFR difference between theoretical model and *in vivo* coronary experiments is 0.06. The dynamic viscosity of blood flow is 4.5 cp.

comparison of pressure drop in figure 3*b*, figure 4*b* shows a Bland–Altman plot for the pairwise comparisons of FFR between the theoretical model and *in vivo* coronary experiments, where the mean ± s.d. of myocardial FFR difference ($FFR_{theory} - FFR_{experiment}$) are 0.01 and 0.06 as well as the r.m.s.e. is 0.06. There was a good agreement of FFR between the theoretical model and *in vivo* coronary experiments.

Figure 5 shows a sensitivity analysis for the distal CSA, stenosis CSA, stenosis length and flow rate in a vessel. The pressure drop was strongly affected by stenosis CSA and flow rate, whereas proximal CSA (not shown), distal CSA and stenosis length had relatively small effects.

4. DISCUSSION

We validate a physics-based model of pressure drop and myocardial FFR for coronary stenosis derived strictly from stenosis dimensions and hyperaemic flow. The proposed analytical model (equation (2.3)) is derived from the general Bernoulli equation with diffusive energy loss and energy loss due to a sudden expansion post-stenosis. The only assumption of the present model is that the flow transition from proximal normal coronary artery to stenosis is well bounded and follows the streamlines so that the pressure loss due to a sudden constriction can be neglected (loss coefficient ≪ 0.1 if there is no plane of vena contracta for the incompressible, laminar coronary blood flow). This assumption is reasonable and consistent with previous models [11–14]. This flow transition results in an approximately uniform distribution of streamlines at the inlet of stenosis so that the flow velocity has a uniform profile, and the entrance effect should be incorporated into the diffusive energy loss, as described in appendix A (also see figure 6*a–c*).

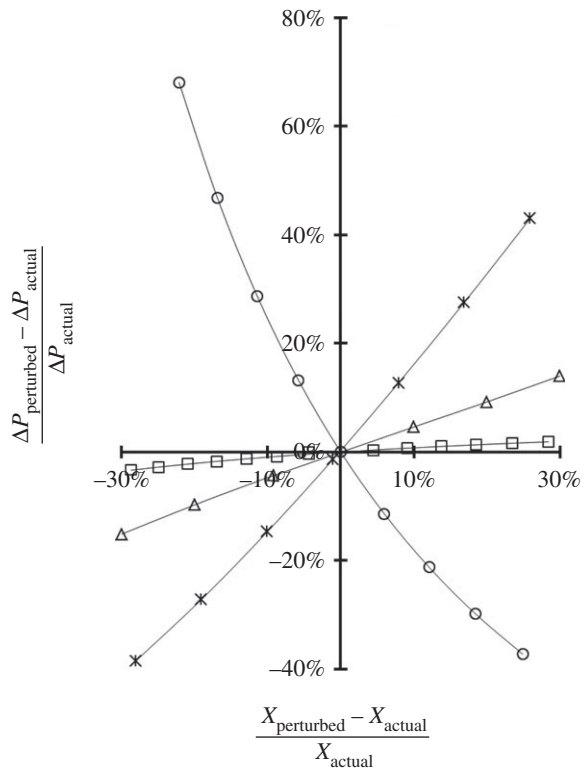

Figure 5. A sensitivity analysis ($X_{\text{perturbed}} - X_{\text{actual}}/X_{\text{actual}}$ versus $\Delta P_{\text{perturbed}} - \Delta P_{\text{actual}}/\Delta P_{\text{actual}}$), where parameter X refers to distal CSA (squares), lesion CSA (circles), lesion length (triangles) and flow rate (asterisks) in a vessel, which have an actual value of $(\pi 4.5^2/4)\,\text{mm}^2$, $(\pi 1.7^2/4)\,\text{mm}^2$, 10 mm and 111 ml min^{-1}. The actual pressure gradient (ΔP_{actual}) equalled to 9.4 mmHg when the dynamic viscosity of flow is 4.5 cp.

The major findings of this study are: (i) the entrance effect at the inlet of a coronary stenosis contributes significantly to the pressure drop (more than half of the total pressure drop across most of the coronary stenoses, with diameters of 0.8–2 mm and lengths of 1–30 mm); (ii) since boundary layer growth stemming from the inlet of stenosis can result in uniform, blunt or parabolic velocity profiles at the outlet of stenosis, the corresponding flow pattern in conjunction with the degree of area stenosis is also an important contributor to the energy loss of sudden expansion; (iii) flow pulsatility and stenosis eccentricity have a negligible effect on FFR in coronary circulation with the relatively low Womersley and Reynolds numbers. These findings are discussed later.

4.1. Comparison of theory and experiments

The uniform and fully developed parabolic velocity profiles at the outlet of stenosis (see equation (2.4)) refer to two states of laminar flows. The uniform velocity underestimates the pressure drop when compared with the fully developed parabolic profile, and both predictions are smaller than measurements (table 3). The pressure drop across a stenosis cannot be accurately predicted, based only on the energy losses caused by the viscosity and sudden expansion at the exit of stenosis. The entrance effect must also be considered, which results in the major difference between the proposed model (equation (2.3)) and previous models [11–14]. The *in vitro* experiments showed a good agreement with the present model predictions (equation (2.3)), as shown in figure 2 and table 3. We found that the pressure drop was significantly underestimated if the entrance effect of stenosis was not considered (e.g. equation (2.4)). Moreover, the last terms ($\Delta P_{\text{expansion}}^{\text{no entrance}}$ in equation (2.4)) cannot have a constant loss coefficient (e.g. 1.52 in a previous study [13]) because it is strongly affected by an interaction of the outlet flow patterns and the degree of stenosis. Here, we used a second-order polynomial interpolation to determine the loss coefficient for the blunt velocity profile that is physically likely in most of coronary stenoses with a diameter of 0.8–2 mm and length of 1–30 mm. The second-order polynomial interpolation physically reflected the growth of flow boundary layer from the inlet to outlet of a coronary stenosis, where the flow velocity may vary from the uniform to parabolic profiles if the stenosis is sufficiently long.

The predictions of equation (2.3) were consistent with those of *in vivo* experiments, as shown in figure 3. Moreover, figure 4 showed that the analytically computed FFR from equations (2.2) and (2.3) agreed reasonably well with those from the *in vivo* coronary experimental measurements using the Volcano ComboWire given the potential error in the measurements. Similar to the previous studies [1,4,23], myocardial FFR computed from equations (2.2) and (2.3) was also found to be less than 0.8 when the area stenosis imposed to a normal coronary artery of swine heart was greater than 0.75. The consistency between theory and *in vitro* and *in vivo* experiments provides some validations of the initial assumptions of uniform and blunt/parabolic flow velocity profiles at the inlet and outlet of a coronary stenosis, respectively, and confirm the significant effects of stenotic entrance region and outlet flow velocity profiles on the pressure drop and FFR.

4.2. Comparison with other studies

Although the Bernoulli equation has many clinical applications [24], it has limited accuracy to predict the pressure drop across a stenosis. For example, the Bernoulli equation predicts a zero pressure drop across a stenosis if the proximal CSA is equal to the distal CSA. The models given by equation (2.4) incorporate the energy loss of viscosity and sudden CSA expansion into the Bernoulli equation, but have been shown to inadequately predict the pressure drop across a stenosis [15]. The present model includes the effects of both entrance region and various outlet flow velocity profiles in coronary stenoses when compared with previous studies that emphasized the energy loss of a sudden expansion at the outlet of stenosis or introduced empirical factors to fit the experimental measurements [11–14,25].

The geometry of stenotic inflow region has been thought to affect the energy loss and hence there has been a significant focus on stenosis morphology [26]. If the change in lumen area is very sharp, which induces a vena contracta, equations (A 4) and (A 5) can be

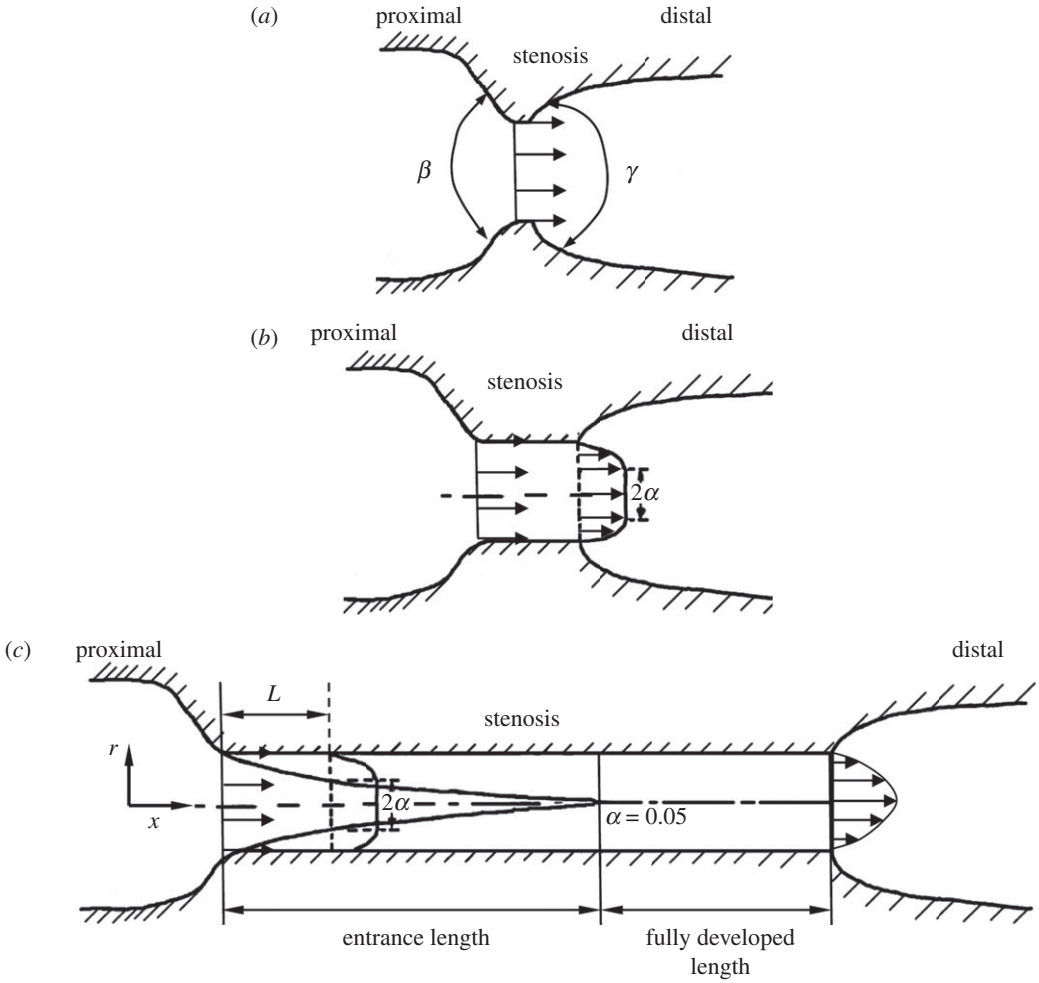

Figure 6. Schematic of (*a*) a thin stenosis, (*b*) a short stenosis and (*c*) a long stenosis.

used to explain the sudden constriction. The growth of a lesion generally follows the streamlines [27,28], however, particularly for the largely laminar blood flow in coronary circulation such that the pressure drop due to the constriction is negligible [18]. This is clearly different from the translational or turbulent flows in aorta stenosis or some peripheral arteries at higher Reynolds numbers [29]. On the other hand, the significance of stenotic entrance region is apparent for the determination of coronary pressure drop and FFR.

The degree of stenosis is disproportionate to CFR and FFR [3,30]. For example, a moderate degree of stenosis added to diffuse narrowing results in a more severe pressure drop than a larger degree of stenosis in a normal vessel [3]. Therefore, the application of classical fluid dynamic principles for the prediction of CFR and FFR has been questioned [30]. This perception is mainly due to the previous analytic models that neglected the entrance effects and simply underscored the pressure drop due to sudden area expansion post-stenosis. In this study, the effects of stenotic entrance were found to account for more than half of the total pressure drop in coronary stenoses with a diameter of 0.8–2 mm and a length of 1–30 mm (figures 2–4). Moreover, the sensitivity analysis in figure 5 showed that the proximal and distal CSAs led to a much smaller pressure drop when compared with the stenotic diameter and flow rate. The foregoing theoretical and experimental results are fundamental to explain why there is a difference between the degree of stenosis and FFR [30] and support the use of geometric dimensions in conjunction with a physics-based model that accounts for the various energy losses (equation (2.3)).

The *in vitro* and *in vivo* measurements of pressure drop and FFR in figures 2–4 show little dependence on stenosis shapes [13,14,31] (e.g. eccentricity, exit angle divergence if $45^\circ \leq$ angle $\gamma \leq 180^\circ$ in figure 6*a* while a vessel with angle $\gamma < 45^\circ$ is not considered as a focal stenosis, entrance shape, etc.). The major reason is that the Reynold and Womersley numbers are relatively small in coronary arteries. This affords a substantial simplification where the proposed model in equation (2.3) does not contain any empirical coefficients and thus overcomes the major shortcoming of previous models that limited patient-specific clinical utility.

We compared the pulsatile flow with the steady-state flow in the *in vitro* experiments. The pressure drop across a stenosis remained relatively unchanged (less than 5%), provided that the mean value of the pulsatile flow rate (time-averaged over a cardiac cycle) equalled the steady-state value. Therefore, the pulsatility of flow has little effect on myocardial FFR because it is

based on the mean value of laminar blood flow and pressure in coronary artery.

4.3. Potential applications of the model

An ischaemic threshold value of FFR has been proposed and confirmed, where a value < 0.75 is associated with inducible ischaemia and a value > 0.80 indicates the absence of ischaemia in the majority of patients [32]. The angiographically based methods for the measurement of coronary flow and lesion dimension are accurate for $7\ \mathrm{ml\,min^{-1}} < Q < 140\ \mathrm{ml\,min^{-1}}$ [6] and $D_{\mathrm{stenosis}} > 1$ mm [8] such that a combination of equations (2.2) and (2.3) can predict FFR for patients.

There have been major developments in cardiac computed tomography angiography (CTA). Coronary CTA has become a routine non-invasive examination for patients with chest pain [33]. Magnetic resonance imaging (MRI) is a useful technique to determine coronary flow [34]. A combination of computational fluid dynamic (CFD) model and CTA and/or MRI can predict the pressure drop across a stenosis [35,36]. This CFD method, however, is time-consuming and requires expertise to ensure the numerical convergence for both steady-state and pulsatile blood flows. The analytical model of equation (2.3) is fast and can be complementary to the CFD model for the non-invasive prediction of FFR.

We have recently introduced a novel catheter-based system (LumenRECON system) to accurately measure coronary lumen CSA [37] and flow velocity [38]. The model of equation (2.3), coupled with the LumenRECON measurements of lumen CSA and flow velocity, can determine FFR and HSR. The stenosis dimensions, coronary flow velocity, FFR and HSR cannot currently be measured with any single device.

4.5. Critique of methods

The analytical model in equation (2.3) was validated experimentally for a single stenosis of various CSAs and lengths. In the presence of serial stenoses, the hyperaemic flow and pressure gradient in the proximal stenosis can be altered by the distal stenosis because the fluid dynamic interaction depends on the sequence, severity and distance between the lesions [2]. For tandem lesions, equation (2.3) needs to be modified to incorporate the attenuation of pressure drop in closely spaced serial stenoses. Myocardial FFR for very severe stenosis (area stenosis $> 95\%$) cannot be accurately estimated by equations (2.2) and (2.3) because there may be significant collateral flow that competes with flow through the stenosis. In such severe lesions, measurements of FFR are not needed.

Because *in vivo* experiments in the present study required a midline sternotomy for placement of the occluder cuff to create different degrees of stenosis, the hyperaemic volumetric flow rate was determined by a flow probe (Transonic Systems Inc.; relative error of $\pm 2\%$ at full scale), which is currently a gold standard. Because angiographic methods for determination of absolute volumetric flow have been validated against direct flow probe measurements [5,6], future closed chest animal studies or human clinical studies can be carried out entirely angiographically to determine non-invasively the FFR. The present study was proof of concept and represents the first critical step in this direction.

4.6. Significance

The present analytical model (equation (2.3)) provides a rationale for prediction of myocardial FFR. This formulation is based on conservation of energy and includes convective and diffusive energy losses and energy loss due to sudden expansion in area. Since the flow transition is well bounded from proximal normal coronary artery to stenosis, there is a uniform distribution of streamlines at the inlet of stenosis (i.e. uniform flow velocity). The entrance energy loss of stenosis is found to be a significant contributor to pressure drop in comparison with previous models, which may explain the disproportionate relationship between the degree of stenosis and FFR from clinical observations [30]. In particular, the present validated analytical model includes no empirical parameters such that it can be used to predict the pressure drop across various dimensions of lesions and future clinical application is warranted.

All animal experiments were performed in accordance with national and local ethical guidelines, including the institute of Laboratory Animal Research Guide, Public Health Service policy, Animal Welfare Act and IUPUI (Indiana University-Purdue University, Indianapolis) polices regarding the use of animals in research.

We thank Dr Xiaomei Guo for excellent technical help.

APPENDIX A

A.1. Diffusive energy loss

The blood flow is largely laminar in coronary arteries because of the low Reynolds number. On the basis of the vessel length, a single stenosis can be divided into three types: (i) a thin orifice (figure 6*a* shows the stenosis length to be nearly zero); (ii) a short stenosis (figure 6*b* shows the entire stenosis to be in the entrance region); (iii) a long stenosis (figure 6*c* shows the stenosis comprised of the entrance and fully developed regions). The diffusive energy loss is generally caused by the viscosity in the fully developed region, as shown in figure 6*c*. However, the pressure drop serves to both accelerate the flow and to overcome viscous drag in the entrance region, which is attributed to the diffusive energy loss in the present study.

The Poiseuille formula is generally applied to blood flow in a fully developed region, which is written as

$$-\mathrm{d}p = \frac{8\pi\mu}{\mathrm{CSA}^2} Q\,\mathrm{d}x, \tag{A 1}$$

where p is the pressure, μ is the dynamic viscosity and Q is the flow rate in the vessel. For the entrance region, we define a dimensionless radius of inviscid core (α), in which the flow velocity is uniform such as $\alpha = r$ at the inlet, $0 < \alpha < r$ from the inlet to the fully developed region, $\alpha = 0$ at the fully developed region, as shown in figure 6*a–c*, respectively. A non-dimensional

entrance length from the inlet ($x = 0$) to a position ($x = L$), as shown in figure 6*c*, can be written as [17]

$$\frac{L}{ReD} = \frac{\pi\mu L}{4\rho Q} = \frac{1}{4}\int_{\alpha}^{1} \frac{(1-\alpha)(6+\alpha)(1+4\alpha+9\alpha^2+4\alpha^3)}{5\alpha(3+2\alpha)(3+2\alpha+\alpha^2)^2}\,\mathrm{d}\alpha, \tag{A 2}$$

where L is the axial distance, D is the inlet diameter and $Re = 4\rho Q/\pi D\mu$ is the Reynolds number. Here, $\alpha = 0.05$ refers to the end of entrance region (i.e. the beginning of fully developed region), as shown in figure 6*c*. Accordingly, the dimensionless pressure drop $((\Delta p)/(\rho Q^2/2\mathrm{CSA}^2))$ in the entrance length (L) is written as [17]

$$\frac{\Delta p}{\rho Q^2/2\mathrm{CSA}^2} = \frac{96}{5}\int_{\alpha}^{1} \frac{(1+4\alpha+9\alpha^2+4\alpha^3)}{\alpha(3+2\alpha)(3+2\alpha+\alpha^2)^2}\,\mathrm{d}\alpha, \tag{A 3}$$

where Δp is the pressure drop in the entrance length (L). Since the stenosis entrance dominates the pressure drop over the normal vessel entrance, the effect of normal vessel entrance can be negligible owing to the relatively large CSA.

A.2. Energy loss due to sudden constriction

When there is a uniform flow velocity at the vessel proximal to the stenosis, the energy loss due to an abrupt constriction in CSAs can be written as [18]

$$\Delta P_{\mathrm{constriction}} = \frac{\rho Q^2}{2}\frac{1}{2}\left(\frac{1}{\mathrm{CSA}_{\mathrm{stenosis}}^{8/3}} - \frac{1}{\mathrm{CSA}_{\mathrm{proximal}}\mathrm{CSA}_{\mathrm{stenosis}}^{5/3}}\right)^{3/4}. \tag{A 4}$$

If the flow velocity profile is parabolic (which is determined by the length of the normal vessel proximal to the stenosis), the energy loss can be written as [39]

$$\Delta P_{\mathrm{constriction}} = \frac{\rho Q^2}{2}\frac{6}{\pi} \times \left(\frac{(1/R_{\mathrm{stenosis}}^4) - (1/R_{\mathrm{stenosis}}^2 R_{\mathrm{proximal}}^2)}{Re_{\mathrm{stenosis}}}\right), \tag{A 5}$$

where $\Delta P_{\mathrm{constriction}}$ is the pressure drop due to an abrupt constriction in CSAs; $\mathrm{CSA}_{\mathrm{stenosis}}$ and $\mathrm{CSA}_{\mathrm{proximal}}$ are the cross-sectional areas and R_{stenosis} and R_{proximal} are the radii at the stenosis and just proximal to the stenosis, respectively; $Re_{\mathrm{stenosis}} = (2\rho Q)/\pi\mu R_{\mathrm{stenosis}}$ is the Reynolds number at the inlet of stenosis. Because the pressure loss of a constriction can be significantly reduced (loss coefficient $\ll 0.1$ generally) with a vessel boundary following the flow streamlines (i.e. there is no plane of vena contracta for the incompressible, laminar coronary blood flow), the energy loss due to a sudden constriction is assumed to be negligible in the present study except for angle $\beta > 150^\circ$ (in figure 6*a*).

A.3. Energy loss due to sudden enlargement

Unlike sudden constriction, there is a large energy loss for sudden enlargement that must be included. If angle $\gamma < 45^\circ$ (in figure 6*a*), we neglect the energy loss because the coronary artery can be clinically presumed to be normal in the absence of diffuse disease. When there is a uniform flow velocity at the outlet of stenosis, the energy loss due to an abrupt expansion in CSA can be determined from the one-dimensional continuity, momentum and energy equations [18], which can be written as

$$\Delta P_{\mathrm{expansion}}^{\mathrm{uniform}} = \frac{\rho Q^2}{2}\left(\frac{1}{\mathrm{CSA}_{\mathrm{stenosis}}} - \frac{1}{\mathrm{CSA}_{\mathrm{distal}}}\right)^2. \tag{A 6}$$

If the flow velocity profile is parabolic at the outlet of stenosis, the energy loss can be written as [40]

$$\Delta P_{\mathrm{expansion}}^{\mathrm{parabolic}} = \rho Q^2\left(\frac{1}{\mathrm{CSA}_{\mathrm{stenosis}}} - \frac{1}{\mathrm{CSA}_{\mathrm{distal}}}\right) \times \left(\frac{1}{\mathrm{CSA}_{\mathrm{stenosis}}} - \frac{1}{3}\frac{1}{\mathrm{CSA}_{\mathrm{distal}}}\right), \tag{A 7}$$

where $\Delta P_{\mathrm{expansion}}$ is the pressure drop due to an abrupt expansion in CSA; $\mathrm{CSA}_{\mathrm{stenosis}}$ and $\mathrm{CSA}_{\mathrm{distal}}$ are the cross-sectional areas at the stenosis and just distal to the stenosis, respectively. If the velocity profile is blunt at the outlet of stenosis (figure 6*b*), the pressure drop will be determined using the interpolation as

$$\Delta P_{\mathrm{expansion}}^{\mathrm{blunt}} = \Delta P_{\mathrm{expansion}}^{\mathrm{uniform}} + \left(\Delta P_{\mathrm{expansion}}^{\mathrm{parabolic}} - \Delta P_{\mathrm{expansion}}^{\mathrm{uniform}}\right) \times (1-\alpha)^2, \tag{A 8}$$

where α is the dimensionless radius of inviscid core.

A.4. Total energy loss across a stenosis

Because the energy loss due to a sudden constriction in CSA has been omitted, the total pressure drop across a stenosis, $\Delta P_{\mathrm{stenosis}}$, can be written as

$$\Delta P_{\mathrm{stenosis}} = \frac{\rho Q^2}{2CSA_{\mathrm{stenosis}}^2} \times \frac{96}{5}\int_{\alpha}^{1} \frac{(1+4\alpha+9\alpha^2+4\alpha^3)}{\alpha(3+2\alpha)(3+2\alpha+a^2)^2}\,\mathrm{d}\alpha + \Delta P_{\mathrm{expansion}}^{\mathrm{blunt}} \quad \text{if } \alpha \geq 0.05 \text{ for } \frac{L_{\mathrm{stenosis}}}{Re_{\mathrm{stenosis}} D_{\mathrm{stenosis}}} \tag{A 9}$$

and

$$\Delta P_{\mathrm{stenosis}} = \frac{\rho Q^2}{2\mathrm{CSA}_{\mathrm{stenosis}}^2}\frac{96}{5}\int_{0.05}^{1} \frac{(1+4\alpha+9\alpha^2+4\alpha^3)}{\alpha(3+2\alpha)(3+2\alpha+a^2)^2}\,\mathrm{d}\alpha + \int_{0}^{L_{\mathrm{stenosis}}-L_{\mathrm{entrance}}} \frac{8\pi\mu}{\mathrm{CSA}_{\mathrm{stenosis}}^2} Q\,\mathrm{d}x + \Delta P_{\mathrm{expansion}}^{\mathrm{parabolic}} \quad \text{if } \alpha < 0.05 \text{ for } \frac{L_{\mathrm{stenosis}}}{Re_{\mathrm{stenosis}} D_{\mathrm{stenosis}}}, \tag{A 10}$$

where L_{stenosis} is the length of stenosis, L_{entrance} is the entrance length with $\alpha = 0.05$ and the length of stenosis

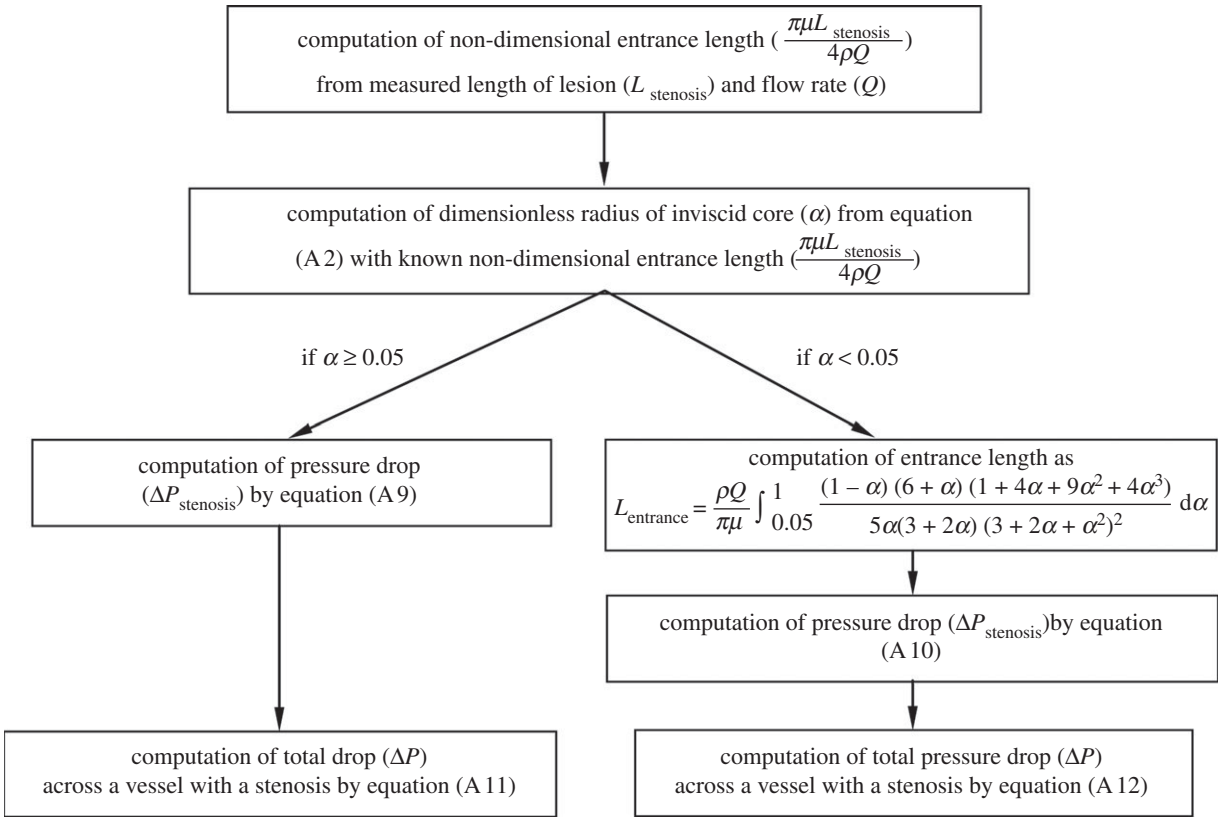

Figure 7. A flow diagram showing steps to determine the total energy loss across a vessel with a stenosis.

minus the entrance length ($L_{\text{stenosis}} - L_{\text{entrance}}$) equals the length of fully developed segment.

A.5. Pressure drop in a vessel with a single stenosis

If the entire length of the stenosis in a vessel (L_{vessel} is the length of vessel, which is composed of both normal vessel and stenosis) is in the entrance region ($\alpha \geq 0.05$ corresponding to equation (A 9)), the total pressure drop across the vessel can be written as

$$\Delta P = \frac{\rho Q^2}{2}\left(\frac{1}{\text{CSA}_{\text{outlet}}^2} - \frac{1}{\text{CSA}_{\text{inlet}}^2}\right) + \frac{\rho Q^2}{2\text{CSA}_{\text{stenosis}}^2}\frac{96}{5} \times \int_{\alpha}^{1} \frac{(1+4\alpha+9\alpha^2+4\alpha^3)}{\alpha(3+2\alpha)(3+2\alpha+a^2)^2}\,d\alpha + \int_{0}^{L_{\text{vessel}}-L_{\text{stenosis}}} \frac{8\pi\mu}{\text{CSA}^2} Q\,dx + \frac{\rho Q^2}{2}\left\{\left(\frac{1}{\text{CSA}_{\text{stenosis}}} - \frac{1}{\text{CSA}_{\text{distal}}}\right)^2 + \left[2\left(\frac{1}{\text{CSA}_{\text{stenosis}}} - \frac{1}{\text{CSA}_{\text{distal}}}\right)\left(\frac{1}{\text{CSA}_{\text{stenosis}}} - \frac{1}{3}\frac{1}{\text{CSA}_{\text{distal}}}\right) - \left(\frac{1}{\text{CSA}_{\text{stenosis}}} - \frac{1}{\text{CSA}_{\text{distal}}}\right)^2\right](1-\alpha)^2\right\}. \quad \text{(A 11)}$$

If the entire length of the stenosis in a vessel includes the entrance and fully developed segments ($\alpha < 0.05$ corresponding to equation (A 10)), the total pressure drop across the vessel can be written as

$$\Delta P = \frac{\rho Q^2}{2}\left(\frac{1}{\text{CSA}_{\text{outlet}}^2} - \frac{1}{\text{CSA}_{\text{inlet}}^2}\right) + \frac{\rho Q^2}{2\text{CSA}_{\text{stenosis}}^2} \times \frac{96}{5}\int_{0.05}^{1} \frac{(1+4\alpha+9\alpha^2+4\alpha^3)}{\alpha(3+2\alpha)(3+2\alpha+a^2)^2}\,d\alpha + \int_{0}^{L_{\text{vessel}}-L_{\text{entrance}}} \frac{8\pi\mu}{\text{CSA}^2} Q\,dx + \rho Q^2\left(\frac{1}{\text{CSA}_{\text{stenosis}}} - \frac{1}{\text{CSA}_{\text{distal}}}\right) \times \left(\frac{1}{\text{CSA}_{\text{stenosis}}} - \frac{1}{3}\frac{1}{\text{CSA}_{\text{distal}}}\right). \quad \text{(A 12)}$$

Equations (A 11) and (A 12) were used to determine the total pressure drop across a vessel with a single stenosis.

A.6. Method of solution

Figure 7 shows a flow diagram for the determination of energy loss across a vessel in the presence of a single stenosis. Briefly, the length of stenosis (L_{stenosis}) and flow rate (Q) are initially used to calculate the non-dimensional entrance length ($L_{\text{stenosis}}/Re_{\text{stenosis}}D_{\text{stenosis}}$ or $\pi\mu L_{\text{stenosis}}/4\rho Q$). The dimensionless radius of inviscid core (α) is then calculated from equation (A 2) with the known non-dimensional entrance ($\pi\mu L_{\text{stenosis}}/4\rho Q$). If $\alpha \geq 0.05$, the entire stenosis is assumed to be in the entrance region, and the pressure drops across the stenosis and vessel can be determined by equations (A 9) and (A 11), respectively. This was the most common scenario, given the dimensions of coronary vessels and lesion lengths. If $\alpha < 0.05$, the entire stenosis can be divided into the entrance and fully developed segments, where

the entrance length L_{entrance} is obtained from equation (A 2) with $\alpha = 0.05$, and the pressure drops across the stenosis and vessel can be determined by equations (A 10) and (A 12), respectively.

REFERENCES

1 Pijls, N. H., van Son, J. A., Kirkeeide, R. L., De Bruyne, B. & Gould, K. L. 1993 Experimental basis of determining maximum coronary, myocardial, and collateral blood flow by pressure measurements for assessing functional stenosis severity before and after percutaneous transluminal coronary angioplasty. *Circulation* **87**, 1354–1367.

2 Kern, M. J. *et al.* 2006 Physiological assessment of coronary artery disease in the cardiac catheterization laboratory: a scientific statement from the American Heart Association Committee on Diagnostic and Interventional Cardiac Catheterization, Council on Clinical Cardiology. *Circulation* **114**, 1321–1341. (doi:10.1161/CIRCULATIONAHA.106.177276)

3 Kern, M. J. & Samady, H. 2010 Current concepts of integrated coronary physiology in the catheterization laboratory. *J. Am. Coll. Cardiol.* **55**, 173–185. (doi:10.1016/j.jacc.2009.06.062)

4 Tonino, P. A. L. *et al.* 2009 Fractional flow reserve versus angiography for guiding percutaneous coronary intervention. *N. Engl. J. Med.* **360**, 213–224. (doi:10.1056/NEJMoa0807611)

5 Molloi, S., Ersahin, A., Tang, J., Hicks, J. & Leung, C. Y. 1996 Quantification of volumetric coronary blood flow with dual-energy digital subtraction angiography. *Circulation* **93**, 1919–1927.

6 Molloi, S., Zhou, Y. & Kassab, G. S. 2004 Regional volumetric coronary blood flow measurement by digital angiography: *in vivo* validation. *Acad. Radiol.* **11**, 757–766.

7 Kassab, G. S. & Molloi, S. 2001 Cross-sectional area and volume compliance of porcine left coronary arteries. *Am. J. Physiol. Heart Circ. Physiol.* **281**, H623–H628.

8 Molloi, S., Kassab, G. S. & Zhou, Y. 2001 Quantification of coronary artery lumen volume by digital angiography: *in vivo* validation. *Circulation* **104**, 2351–2357. (doi:10.1161/hc4401.098435)

9 Hoffman, J. I. & Spaan, J. A. 1990 Pressure-flow relations in coronary circulation. *Physiol. Rev.* **70**, 331–390.

10 Siebes, M., Verhoeff, B.-J., Meuwissen, M., de Winter, R. J., Spaan, J. A. E. & Piek, J. J. 2004 Single-wire pressure and flow velocity measurement to quantify coronary stenosis hemodynamics and effects of percutaneous interventions. *Circulation* **109**, 756–762. (doi:10.1161/01.CIR.0000112571.06979.B2)

11 Young, D. F. & Tsai, F. Y. 1973 Flow characteristics in models of arterial stenoses. I. Steady flow. *J. Biomech.* **6**, 395–410. (doi:10.1016/0021-9290(73)90099-7)

12 Young, D. F. & Tsai, F. Y. 1973 Flow characteristics in models of arterial stenoses. II. Unsteady flow. *J. Biomech.* **6**, 547–559. (doi:10.1016/0021-9290(73)90012-2)

13 Seeley, B. D. & Young, D. F. 1976 Effect of geometry on pressure losses across models of arterial stenoses. *J. Biomech.* **9**, 439–448. (doi:10.1016/0021-9290(76)90086-5)

14 Young, D. F., Cholvin, N. R., Kirkeeide, R. L. & Roth, A. C. 1977 Hemodynamics of arterial stenoses at elevated flow rates. *Circ. Res.* **41**, 99–107.

15 Gould, K. L. 1980 Dynamic coronary stenosis. *Am. J. Cardiol.* **45**, 286–292. (doi:10.1016/0002-9149(80)90647-5)

16 Nichols, W. W. & O'Rourke, M. F. 2005 *McDonald's blood flow in arteries: theoretical, experimental and clinical principles*, 5th edn. London, UK: Hodder Arnold.

17 Fargie, D. & Martin, B. W. 1971 Developing laminar flow in a pipe of circular cross-section. *Proc. R. Soc. Lond. A* **321**, 461–476. (doi:10.1098/rspa.1971.0043)

18 Miller, D. S. 1990 *Internal flow systems: design and performance prediction*, 2nd edn. Cranfield, UK: British Hydromechanics Research Association.

19 Huo, Y., Choy, J. S., Svendsen, M., Sinha, A. K. & Kassab, G. S. 2009 Effects of vessel compliance on flow pattern in porcine epicardial right coronary arterial tree. *J. Biomech.* **42**, 594–602. (doi:10.1016/j.jbiomech.2008.12.011)

20 Huo, Y., Wischgoll, T. & Kassab, G. S. 2007 Flow patterns in three-dimensional porcine epicardial coronary arterial tree. *Am. J. Physiol. Heart Circ. Physiol.* **293**, H2959–H2970. (doi:10.1152/ajpheart.00586.2007)

21 Zheng, H., Huo, Y., Svendsen, M. & Kassab, G. S. 2010 Effect of blood pressure on vascular hemodynamics in acute tachycardia. *J. Appl. Physiol.* **109**, 1619–1627. (doi:10.1152/japplphysiol.01356.2009)

22 Choy, J. S. & Kassab, G. S. 2009 Wall thickness of coronary vessels varies transmurally in the LV but not the RV: implications for local stress distribution. *Am. J. Physiol. Heart Circ. Physiol.* **297**, H750–H758. (doi:10.1152/ajpheart.01136.2008)

23 de Bruyne, B., Bartunek, J., Sys, S. U., Pijls, N. H. J., Heyndrickx, G. R. & Wijns, W. 1996 Simultaneous coronary pressure and flow velocity measurements in humans: feasibility, reproducibility, and hemodynamic dependence of coronary flow velocity reserve, hyperemic flow versus pressure slope index, and fractional flow reserve. *Circulation* **94**, 1842–1849.(doi:10.1161/01.CIR.94.8.1842)

24 Braunwald, E., Zipes, D. P., Libby, P. & Bonow, R. 2004 *Braunwald's heart disease: a textbook of cardiovascular medicine, single volume*, 7th edn. London, UK: Saunders.

25 Collins, S. & Skorton, D. 1986 *Cardiac imaging and image processing*. New York, NY: McGraw Hill.

26 Strony, J., Beaudoin, A., Brands, D. & Adelman, B. 1993 Analysis of shear stress and hemodynamic factors in a model of coronary artery stenosis and thrombosis. *Am. J. Physiol. Heart Circul. Physiol.* **265**, H1787–H1796.

27 Stary, H. C. *et al.* 1992 A definition of the intima of human arteries and of its atherosclerosis-prone regions. A report from the Committee on Vascular Lesions of the Council on Arteriosclerosis, American Heart Association. *Arterioscler. Thromb. Vas. Biol.* **12**, 120–134. (doi:10.1161/01.ATV.12.1.120)

28 Stary, H. C. *et al.* 1995 A definition of advanced types of atherosclerotic lesions and a histological classification of atherosclerosis. A report from the Committee on Vascular Lesions of the Council on Arteriosclerosis, American Heart Association. *Circulation* **92**, 1355–1374.

29 Berger, S. A. & Jou, L.-D. 2000 Flows in stenotic vessels. *Annu. Rev. Fluid. Mech.* **32**, 347–382. (doi:10.1146/annurev.fluid.32.1.347)

30 Gould, K. L. 2009 Does coronary flow trump coronary anatomy? *J. Am. Coll. Cardiol. Img.* **2**, 1009–1023.

31 Lipscomb, K. & Hooten, S. 1978 Effect of stenotic dimensions and blood flow on the hemodynamic significance of model coronary arterial stenoses. *Am. J. Cardiol.* **42**, 781–792. (doi:10.1016/0002-9149(78)90098-X)

32 Pijls, N. H., De Bruyne, B., Peels, K., van der Voort, P. H., Bonnier, H. J. R. M., Bartunek, J. & Koolen, J. J. 1996 Measurement of fractional flow reserve to assess the functional severity of coronary-artery stenoses. *N. Engl. J. Med.* **334**, 1703–1708. (doi:10.1056/NEJM199606273342604)

33 Chun, E. J. *et al.* 2008 Effects of nitroglycerin on the diagnostic accuracy of electrocardiogram-gated coronary computed tomography angiography. *J. Comput. Assist. Tomogr.* **32**, 86–92. (doi:10.1097/rct.0b013e318059befa)

34 Lund, G. K., Watzinger, N., Saeed, M., Reddy, G. P., Yang, M., Araoz, P. A., Curatola, D., Bedigian, M. & Higgins, C. B. 2003 Chronic heart failure: global left ventricular perfusion and coronary flow reserve with velocity-encoded cine MR imaging: initial results. *Radiology* **227**, 209–215. (doi:10.1148/radiol.2271012156)

35 Steinman, D. A., Thomas, J. B., Ladak, H. M., Milner, J. S., Rutt, B. K. & Spence, J. D. 2002 Reconstruction of carotid bifurcation hemodynamics and wall thickness using computational fluid dynamics and MRI. *Magn. Reson. Med.* **47**, 149–159. (doi:10.1002/mrm.10025)

36 Steinman, D. A. 2002 Image-based computational fluid dynamics modeling in realistic arterial geometries. *Ann. Biomed. Eng.* **30**, 483–497. (doi:10.1114/1.1467679)

37 Kassab, G. S., Choy, J. S., Svendsen, M., Sinha, A. K., Alloosh, M., Sturek, M., Huo, Y., Sandusky, G. E. & Hermiller, J. 2009 A novel system for the reconstruction of a coronary artery lumen profile in real time: a preclinical validation. *Am. J. Physiol. Heart Circ. Physiol.* **297**, H485–H492. (doi:10.1152/ajpheart.01224.2008)

38 Zhang, Z.-D., Svendsen, M., Choy, J. S., Sinha, A. K., Huo, Y., Yoshida, K., Molloi, S. & Kassab, G. S. 2011 New method to measure coronary velocity and coronary flow reserve. *Am. J. Physiol. Heart Circ. Physiol.* **301**, H21–H28. (doi:10.1152/ajpheart.00080.2011)

39 Sisavath, S., Jing, X., Pain, C. C. & Zimmerman, R. W. 2002 Creeping flow through an axisymmetric sudden contraction or expansion. *J. Fluids Eng.* **124**, 273–278. (doi:10.1115/1.1430669)

40 Oliveira, P. J. & Pinho, F. T. 1997 Pressure drop coefficient of laminar Newtonian flow in axisymmetric sudden expansions. *Int. J. Heat Fluid Flow* **18**, 518–529.